11-30-2006

Effect of Nb and C Additives on the Microstructures and Magnetic Properties of Rapidly Solidified Sm-Co Alloys

S. Aich
University of Nebraska - Lincoln

Jeffrey E. Shield
University of Nebraska - Lincoln, jshield@unl.edu

Published in *Journal of Alloys and Compounds* **425**:1-2 (November 30, 2006), pp. 416-423; doi:10.1016/j.jallcom.2006.01.067

Submitted November 29, 2005; revised January 24, 2006; accepted January 28, 2006; published online March 3, 2006.

Effect of Nb and C additives on the microstructures and magnetic properties of rapidly solidified Sm–Co alloys

S. Aich* and J.E. Shield

Department of Mechanical Engineering and Center for Materials Research and Analysis, University of Nebraska–Lincoln, Lincoln, NE 68588, United States

**Corresponding author: tel.* 402 472-4206; *fax* 402 472-1465

Abstract

Highly coercive Sm-Co-based permanent magnets have been achieved through simple modification of binary $Sm_{12}Co_{88}$ alloys with Nb, C or combined Nb and C at concentrations ranging from 1 to 10 atomic percent processed via rapid solidification. Melt spinning at 40 m/s resulted in the formation of the metastable $TbCu_7$-type structure in all alloys. While the unalloyed, as-solidified $Sm_{12}Co_{88}$ alloy displayed a coercivity of 0.5 kOe, alloying additions resulted in a systematic and profound increase in coercivity. Nb additions resulted in as-solidified coercivities up to 9 kOe, C additions up to 37 kOe, and combined NbC additons 8 kOe. The Nb and NbC additions led to a reduction in grain size, while C additions altered the morphology, producing a grain-boundary phase that effectively isolated the magnetic grains from one another. The magnetization processes for Nb- and NbC-modified Sm–Co were determined to be nucleation-controlled, while a transition to pinning-controlled magnetization was observed for the C-modified alloy.

Keywords: microstructure, permanent magnets, alloying additions, coercivity, rapid solidification

PACS classification codes: 75.01A; 89.02; 07.55; 85.70

1. Introduction

Sm–Co-based magnets have drawn attention since the early 1970s for their highly attractive properties, such as high energy density (15–30 MGOe), reliable coercive force, best high-temperature performance and relatively good corrosion and oxidation resistance. These properties have made Sm–Co as the ideal material in dynamic applications such as generators and motors, as well as in demanding environments. The Sm–Co system forms two related equilibrium phases in Co-rich compositions: the $CaCu_5$-type $SmCo_5$ structure and the Th_2Zn_{17}-type Sm_2Co_{17} structure [1,2]. The unit cell parameters are related, with $c_{2:17} = 3c_{1:5}$ and $a_{2:17} = (3a_{1:5})^{½}$. In addition to the ordered Sm_2Co_{17} dumbbell structures, a disordered variant of the Th_2Zn_{17}-type structure is available which is $TbCu_7$-type $SmCo_7$ structure where Sm and Co–Co dumbbell pairs randomly occupy the rare earth sites [2]. This metastable structure has the same unit cell as the $CaCu_5$ structure. In 2:17 type precipitation-hardened $Sm(Co,Fe,Cu,Zr)_z$ magnets, after a complex heat-treatment, the high coercivity originates due to the formation of complex microstructures consisting of cellular and lamellar phases [3–8]. The cellular microstructures represent the rhombohedral $Sm_2(Co,Fe)_{17}$ cells (~50–100 nm) surrounded by Cu-rich $Sm(Co,Cu)_5$ phase at the cell boundaries (thickness ~10 nm). The lamellar microstructures consist of a Zr-rich hexagonal 2:17 phase which is superimposed on the cellular microstructures. Moreover the 2:17 type magnets are stable up to 300 °C. Nanocrystalline SmCo-1:7 materials can be operated stably at 500 °C by adding ZrB_2 without any complex heat-treatment [9].

However, the microstructures and the magnetic properties obtained are strongly dependent on the alloy composition, processing parameters and heat-treatments. Rapidly solidified melt-spun ribbons of Sm–Co alloys have exhibited higher anisotropy, improved microstructures and better magnetic properties. High M_r (8.5 kG) and H_c (4.1 kOe) were observed in isotropic ribbons, whereas the anisotropic ribbons achieved $(BH)_{max}$ as high as 18.2 MGOe and a high remanence ratio of 0.9 [10,11]. Zr and Cu substitution for Co helped to reduce the crystallographic texture in $Sm(Co_{0.74}Fe_{0.1}Zr_{0.04}Cu_{0.12})_{8.5}$ rib-

bons which were nearly isotropic [12]. In Fe-rich $SmCo_5Fe_x$ (x = 0, 1 and 2) melt-spun ribbons, produced by using a wheel speed of 25 m/s, the higher surface to volume ratio due to the smallest grain size in x = 2 ribbons exhibited enhanced remanence due to improved inter-grain exchange coupling [13]. Higher magnetic properties (coercivity as high as 38.5 kOe) were reported for melt-spun $Sm(Co_{0.74-x}Fe_{0.1}Cu_{0.12}Zr_{0.04}B_x)_{7.5}$ (x = 0.005–0.05) alloys [14]. Better magnetic properties were reported for the boron containing samples than the carbon containing samples in melt-spun $Sm(CoFeCuZr)_zM_x$ (M = B or C) nanocomposite magnets due to the finer grain size (30–50 nm) of the former [15].

There is strong interest in generating highly coercive materials without the complex heat treatments necessary for magnets produced by classic powder metallurgical approaches [16,17]. In this research, we report the structure and magnetic properties of rapidly solidified SmCo permanent magnets of simple binary alloy systems modified with Nb and C additions.

2. Experimental procedures

Alloys with nominal compositions of $(Sm_{0.12}Co_{0.88})_{100-x}Nb_x$, $(Sm_{0.12}Co_{0.88})_{100-y}C_y$, and $(Sm_{0.12}Co_{0.88})_{100-(x+y)}Nb_xC_y$ with x and y from 0 to 10 were made from high purity (>99.95%) elements by arc-melting in a high purity argon atmosphere. Before arc-melting 5% extra Sm was added to the sample to compensate for loss due to Sm vaporization during melting. The ingot was then rapidly solidified by melt spinning in high-purity argon at a chamber pressure of 1 atm and a tangential wheel velocity of 40 m/s.

The samples were analyzed by X-ray diffraction using a Philips X-ray diffractometer with Cu Kα radiation. The powdered samples were mounted on an off-cut SiO_2 single crystal to avoid the diffraction effects of the sample holder, or an amorphous SiO_2 slide. X-ray data were fit using Rietveld analysis utilizing Siroquant software. Both of the lattice parameters "c" and "a" were determined from the X-ray diffraction patterns using SIRQUANT software. The magnetic measurements were made by SQUID magnetometry at 300 K utilizing a Quantum Design MPMS with maximum field of 7 T. Magnetic measurements were made on several ribbon pieces mounted so that the magnetic field was applied in the plane of the ribbon. Transmission electron microscopy was accomplished with a JEOL2010 operating at 200 kV. Electron transparency was achieved by mounting the melt-spun ribbon on a slightly polished Cu oval and by ion milling to perforation using a Gatan Duomill or PIPS at 4.5 kV.

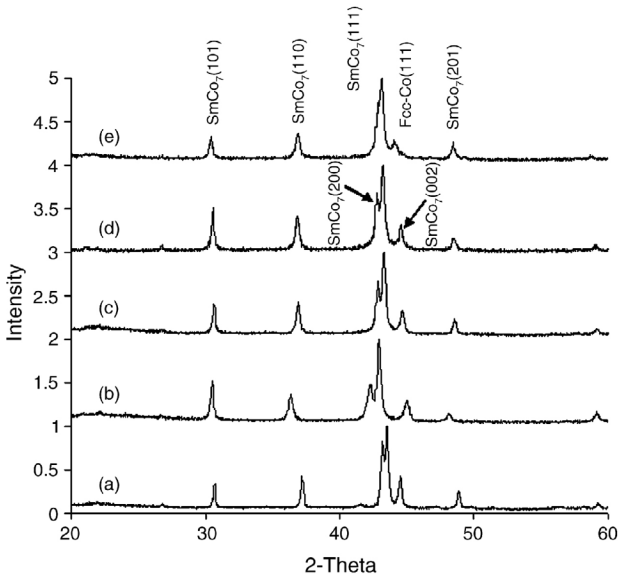

Figure 1. X-ray diffraction scans of $(Sm_{12}Co_{88})_{100-x}Nb_x$ alloy melt spun at 40 m/s for x = 0, 1, 2, 3 and 5 (from (a) to (e)). Peaks were indexed to the $SmCo_7$ structure.

3. Results and discussion

3.1. Effects of niobium additions

$(Sm_{0.12}Co_{0.88})_{100-x}Nb_x$ with x = 0, 1, 2, 3 and 5 and melt spun at 40 m/s resulted in the formation of the metastable $TbCu_7$-type $SmCo_7$ structure at all values of x (Figure 1). The equilibrium Sm_2Co_{17} structure with the Th_2Zn_{17}-type structure is most easily identified by the (0 2 4) superlattice peak that appears at approximately 37.8° 2θ. This peak was not observed in any of the X-ray diffraction patterns. The indexing scheme of Figure 1 (and throughout this paper) therefore refers to the hexagonal $TbCu_7$-type structure (space group P6/mmm [18]). At higher values of x, a diffraction peak indexing to fcc Co appears. Peak broadening also increases as x increases, suggesting a refinement in grain size. However, the broadening may also arise from topological disorder arising from the chemical disorder (i.e., misplaced transition metal dumbbell atoms) in the structure.

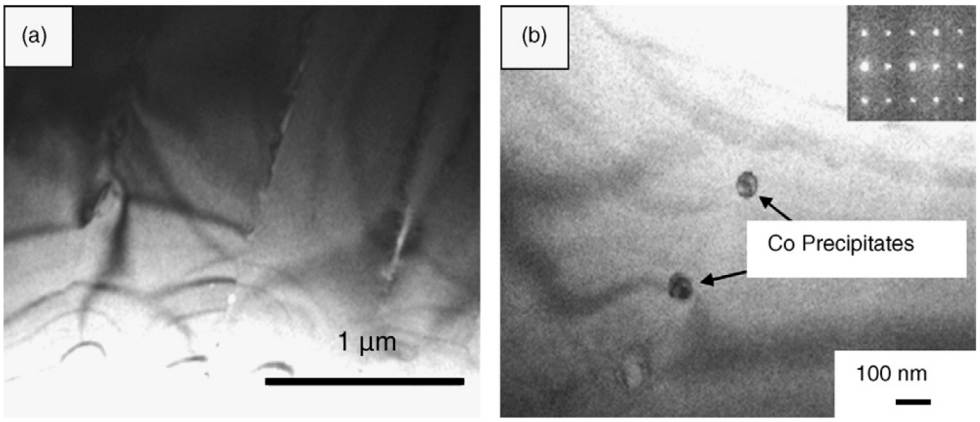

Figure 2. Transmission electron micrographs revealing the microstructures of the $(Sm_{12}Co_{88})_{100-(x+y)}Nb_xC_y$ alloy melt-spun at 40 m/s (a) for x, y = 0,0 showing large 1:7 grains, (b) for x, y = 0,0 showing Co precipitates ~80 nm.

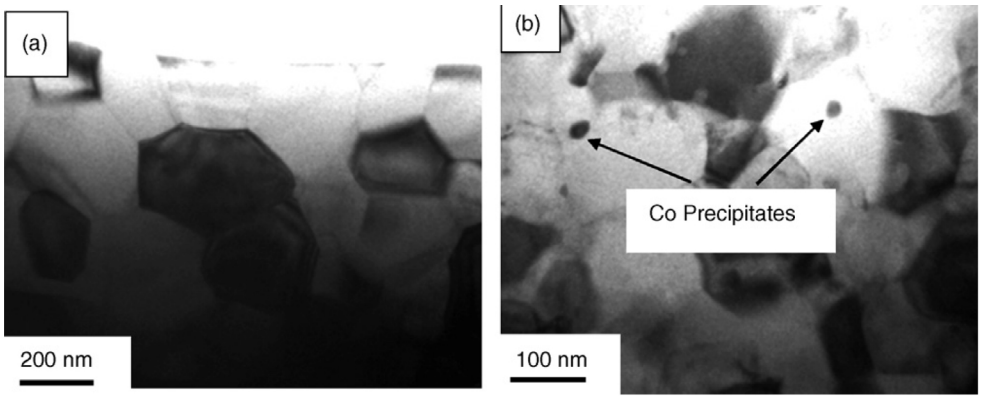

Figure 3. Transmission electron micrographs revealing the microstructure of the $(Sm_{12}Co_{88})_{100-x}Nb_x$ alloy melt-spun at 40 m/s (a) for $x = 1$ showing equiaxed smaller 1:7 grains and (b) for $x = 5$ showing equiaxed 1:7 grains relatively smaller in size with a few scattered black spots.

Transmission electron microscopy investigations revealed that the Nb additions resulted in a refinement in grain size. TEM revealed that the binary alloy ($x = 0$) had a very coarse grain size of ~1 μm for the $SmCo_7$ phase (Figure 2(a)). In addition, ~80 nm precipitates were observed (Figure 2(b)). Electron diffraction revealed that these were fcc Co. The rather large grain size was somewhat surprising, given the rapid solidification processing. The formation of Co was also not expected, considering the equilibrium phase diagram [19]. The Co evidently forms due to the non-equilibrium processing, as the solidification follows metastable extensions of the liquidus and solidus lines [20]. Its presence in binary Sm–Co alloys also deleteriously affects magnetic properties [21]. The Co was not observed in the X-ray diffraction patterns due to its low volume fraction. The addition of Nb resulted in a refinement of the $SmCo_7$ grains, with the grain size of the $x = 5$ alloy decreasing to 75 nm (Figure 3). In addition, alloying with Nb apparently eliminated the formation of Co, at least at smaller values of x, as no Co precipitates were observed. The exception is $x = 5$, where some ~20 nm Co precipitates were observed.

The magnetic properties were also profoundly influenced by the addition of Nb. The coercivity of the sample with $x = 0$ was only 500 Oe, but increased with increasing x (Figure 4). The increase in coercivity reflected the microstructural changes, notably the decrease in grain size but also the elimination of Co. The grain size was reduced below the single domain limit, (approximately 500 nm for these alloys). The observation of a high coercivity at $x = 5$ even with Co present is likely due to the refinement of the Co, which allows intergranular exchange coupling with the hard magnetic grains, alleviating the detrimental influence it normally has on the magnetic properties. This also suggests that the grain size of the $SmCo_7$ phase is most critical in coercivity improvement. For the alloy with $x = 2$, the coercivity dropped to 3.4 kOe; the reason for this drop is the microstructural changes occurred during solidification.

The initial magnetization curves were also measured in order to gain an understanding of the magnetization process. Figure 5 shows that all alloys displayed a steep linear response to the applied magnetic field, suggesting that nucleation processes dominate the magnetization process. The exception could be $x = 0$, where the grain size was larger, and in the absence of structural defects a steep initial magnetization curve could indicate easy domain-wall motion. The slope is not dependent on composition, again indicating that the different alloys behave similarly to one another. The curve for $x = 5$ has a slight deflection, perhaps suggesting the presence of domain-wall processes, but it is not clear enough to clearly identify domain-wall magnetization processes.

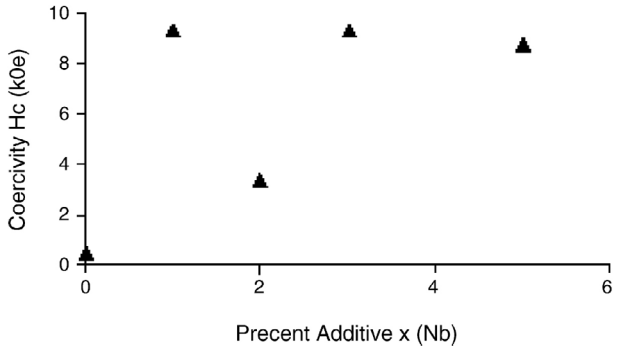

Figure 4. Relationship between percent additive x and intrinsic coercivity for the $Sm_{12}Co_{88}$ alloys—40 m/s modified with Nb (▲).

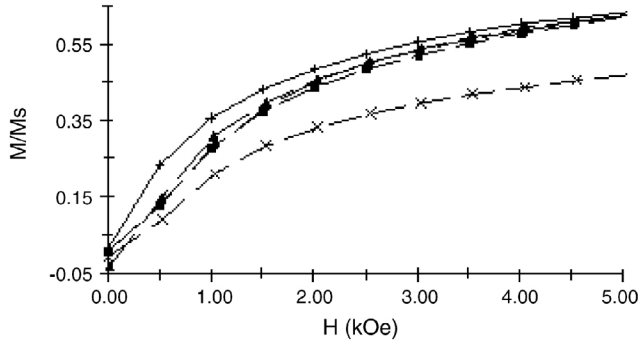

Figure 5. The normalised curves showing initial magnetization processes for the $(Sm_{12}Co_{88})_{100-x}Nb_x$—40 m/s alloys at different x values, $x = 1$ (♦), $x = 2$ (▲), $x = 3$ (■) and $x = 5$(×). The curve (+) is indicating the sample without any additive.

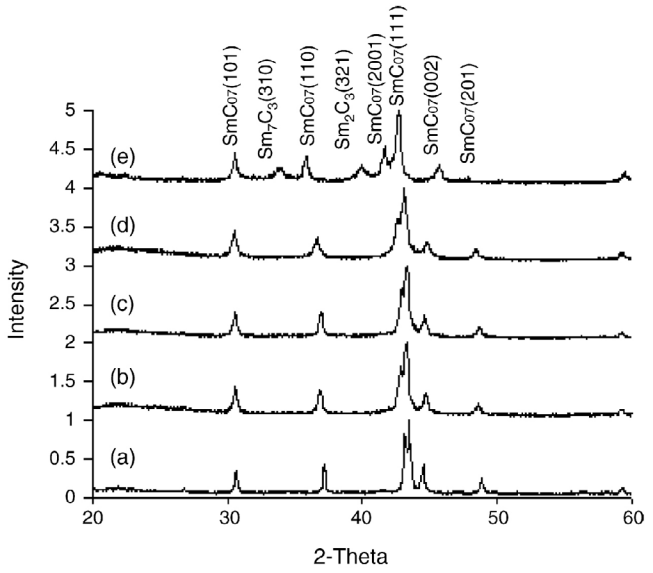

Figure 6. X-ray diffraction scans of $(Sm_{12}Co_{88})_{100-y}C_y$ alloy melt spun at 40 m/s for $y = 0$, 1, 2, 3 and 5 (from (a) to (e)). Peaks were indexed to the $SmCo_7$ structure.

3.2. Effects of C additions

$(Sm_{0.12}Co_{0.88})_{100-y}C_y$ with $y = 0$, 1, 2, 3 and 5 and melt spun at 40 m/s resulted in the formation of the metastable $TbCu_7$-type $SmCo_7$ structure at all values of x (Figure 6). As with the Nb additions, no evidence of the ordered Sm_2Co_{17} structure was observed (namely, the (0 2 4) superlattice peak). At higher C content ($y = 5$), peaks corresponding to the Sm_2C_3 phase were observed.

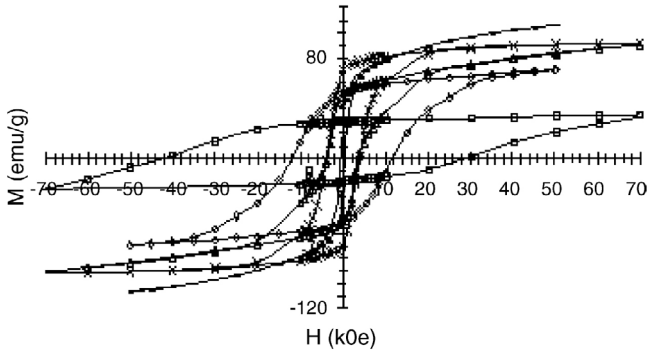

Figure 8. Hysteresis loops of $(Sm_{12}Co_{88})_{100-y}C_y$ alloy melt spun at 40 m/s for $y = 0$ (–), 1 (Δ), 2 (×), 3 (◊) and 5 (□).

The carbon additions also profoundly altered the microstructure. At low values of y, some grain refinement was observed, and the grains were predominantly equiaxed (Figure 7). At $y = 3$, a distinct grain-boundary phase was observed, with a thickness of a few nanometers (Figure 7(b)). While the fine scale precluded definite identification, presumably the intergranular phase is Sm_2C_3. The overall morphology remained equiaxed. At $y = 5$, a distinct change in morphology occurred, with a dendritic structure predominant (Figure 7(c)). The dendrite widths were on the order of 50 nm. As with Nb additions, C additions eliminated the formation of primary solidified Co.

The addition of C greatly improved the coercivity and decreased the saturation magnetization (Figure 8). The improvement in coercivity was related to the concentration of C (Figure 9), and reached a maximum of 37 kOe at $y = 5$. However, it is likely that the coercivity is actually higher, as the hystere-

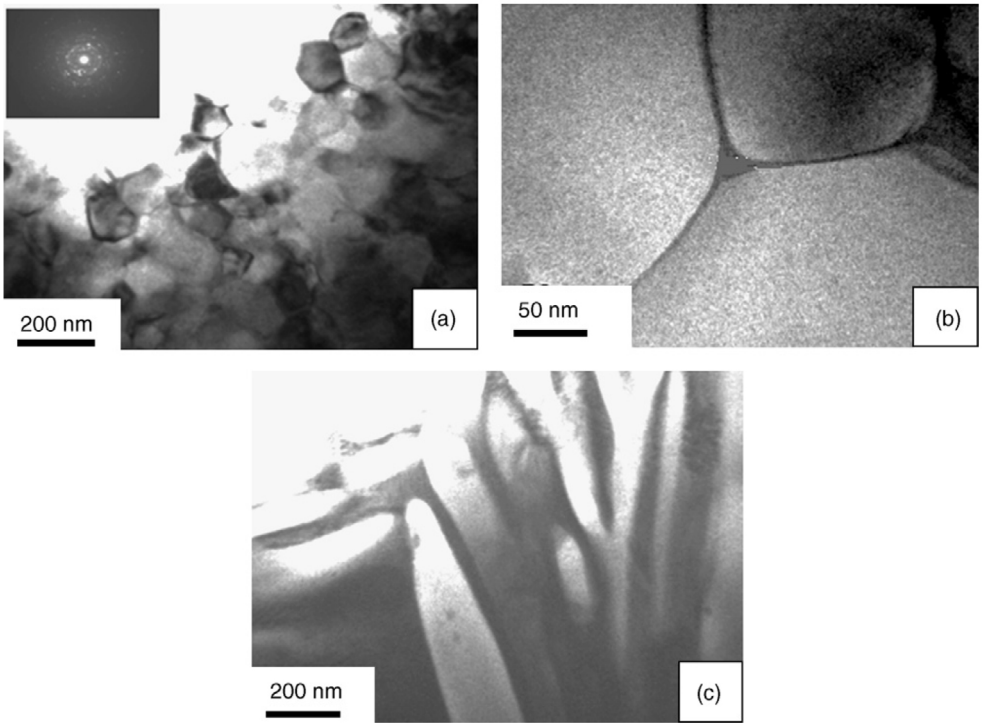

Figure 7. Transmission electron micrograph revealing the microstructure of the $(Sm_{12}Co_{88})_{100-(x+y)}Nb_xC_y$ alloy melt-spun at 40 m/s (a) for $x = 0$, $y = 1$ showing equiaxed grains (top left inset shows the electron diffraction pattern), (b) for $x = 0$, $y = 3$ a nice triple point grain boundary and (c) for $x = 0$, $y = 5$ showing dendritic structures.

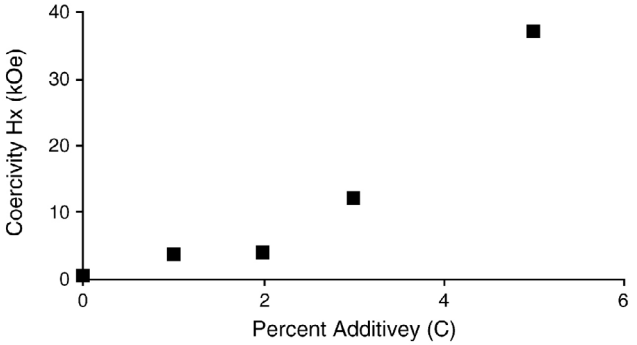

Figure 9. Relationship between percent additive *y* and intrinsic coercivity for the $Sm_{12}Co_{88}$ alloys—40 m/s modified with C (■).

sis loop did not completely close. Higher applied fields would be necessary to determine the coercive force for $y = 5$. The increase in coercivity at low values of *y* is attributed to a reduction in grain size, while the substantial increase at $y = 3$ and 5 is most likely due to the Sm_2C_3 grain-boundary phase. Sm_2C_3 wets the grain boundaries, isolating the grains from one another which decrease the magnetostatic interactions. The saturation magnetization decreased with increasing *y*. While the decrease at higher *y* is easily attributed to the formation and increasing volume fraction of a non-magnetic second phase, the decrease at low *y* may be due to intrinsic changes caused by C dissolution in the $SmCo_7$ structure.

The initial magnetization curves also reflected different magnetization processes at low and high values of *y* (Figure 10). At low *y*, the material had a steep response to the applied magnetic field, consistent with nucleation-controlled processes and similar to the Nb-modified alloys. At higher values of *y*, there was a clear inflection in the initial magnetization curves. At low fields, the materials displayed a weak response to the applied field. This gave way to a rapid increase at a higher applied field. This type of behavior is more closely associated with domain-wall dominated magnetization processes. No structural defects that could act as domain-wall pinning sites were observed in the grain interiors in the TEM micrographs. The pinning sites could lie at grain boundaries. In addition, the very smooth grain boundaries may inhibit nucleation events, allowing domain-wall processes to dominate.

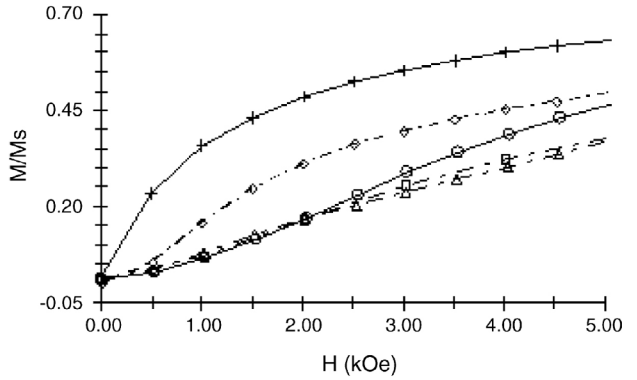

Figure 10. The normalized curves showing initial magnetization processes for the $(Sm_{12}Co_{88})_{100-y}C_y$–40 m/s alloys modified with C at different *y* values $y = 1$ (—◊—), $y = 2$ (—Δ—), $y = 3$ (—□—), and $y = 5$ (¤) and (+) is indicating the sample without any additive.

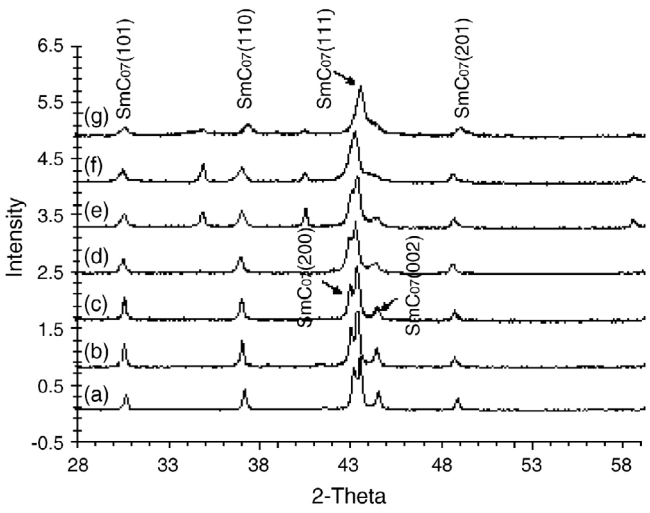

Figure 11. X-ray diffraction scans of $(Sm_{12}Co_{88})_{100-(x+y)}Nb_xC_y$ alloy melt spun at 40 m/s for $x = y = 0$, 1, 2, 3, 5, 7 and 10 (from (a) to (g)). Peaks were indexed to the $SmCo_7$ structure.

3.3. Effects of combined niobium and carbon additions

As with the single alloying additions of Nb and C, combined Nb and C additions to Sm–Co in the form $(Sm_{0.12}Co_{0.88})_{100-2x}(NbC)_x$ resulted in the formation of the $TbCu_7$-type disordered structure for all but the highest values of *x* and *y* after melt spinning at a tangential wheel speed of 40 m/s (Figure 11). Except at $x = 10$, no evidence of the ordered Sm_2Co_{17} structure was observed in the X-ray diffraction patterns. At $x \geq 5$, peaks corresponding to the NbC phase were observed (Figure 12). This provides a good estimate of the solubility of NbC in the liquid; at higher concentrations, the NbC precipitates out of the liquid. At $x = 10$, the (0 2 4) Sm_2Co_{17} superlattice peak was observed. It is not clearly understood why only this alloy displayed long-range order. Since the development of order is related to solidification rate, the alloying content may have altered the solidification process enough to allow the equilibrium ordered structure to form.

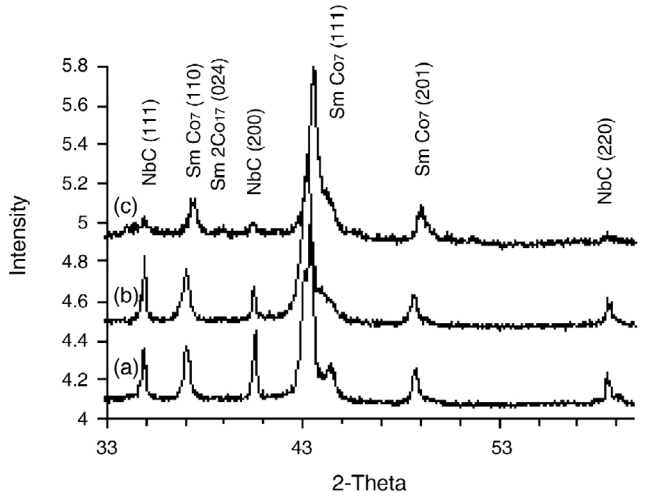

Figure 12. X-ray diffraction scans of $(Sm_{12}Co_{88})_{100-(x+y)}Nb_xC_y$ alloy melt spun at 40 m/s for *x*, *y* = (5,5), (7,7) and (10,10) (from (a) to (c)).

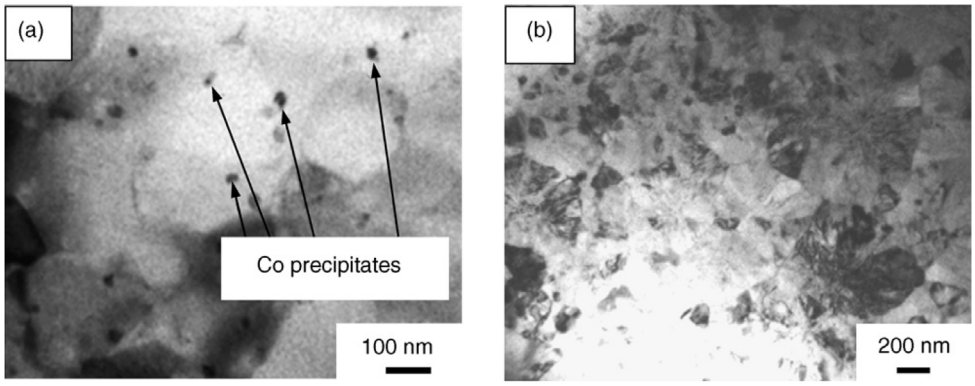

Figure 13. Transmission electron micrograph revealing the microstructure of the $(Sm_{12}Co_{88})_{100-(x+y)}Nb_xC_y$ alloy melt-spun at 40 m/s (a) for $x, y = 3, 3$ showing large 1:7 grains and scattered Co precipitates ~10 nm and (b) for $x, y = 7, 7$ showing very small sized grains.

The combined addition of Nb and C influenced the microstructure as well, as revealed through TEM investigations. Primarily, a reduction in grain size was observed (Figure 13). The grain refinement was related to the concentration of NbC, decreasing monotonically for $x = 1–7$, and then increasing for $x = 10$. The increase in grain size again suggests that the solidification process was altered for $x = 10$. An equiaxed grain structure was evident at all values of x. However, unlike the single addition Sm–Co–Nb and Sm–Co–C alloys, the formation of Co was not suppressed by the combined NbC addition. However, the scale of the Co was significantly reduced to approximately 10 nm. The volume fraction of Co was estimated to be 3–5 volume percent from the TEM micrographs, which is roughly the limit for detection using X-ray diffraction. At higher values of x, formation of NbC formation along grain boundaries was observed.

At the nanometer scale, the Co is effectively magnetically coupled to the hard magnetic $SmCo_7$ phase and thus is not expected to be as detrimental to the magnetic properties as the larger Co precipitates were in the binary Sm–Co alloy. Indeed, an increase in coercivity was observed upon the addition of NbC. A monotonic increase in coercivity with NbC content was observed for $x = 1–7$, which was followed by a sharp decrease in coercivity at $x = 10$ (Figure 14). The decrease was likely related to the increase in grain size observed for the alloy with $x = 10$. Indeed, the coercivity fit well in the overall relationship between grain size and coercivity, with a coercive force between the samples with $x = 1$ and 3, which bracket the $x = 10$ sample with respect to grain size (Figure 15). The initial magnetization curves displayed nucleation-dominated processes at low x (Figure 16). As x increased, some inflection was observed, suggesting contributions to the magnetization from domain-wall processes. However, the inflections were not as pronounced as the Sm–Co–C alloys.

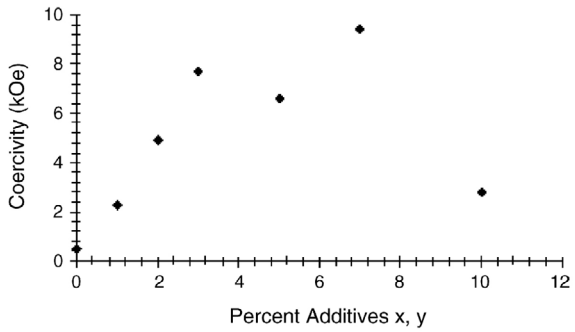

Figure 14. Relationship between percent additives x and y and intrinsic coercivity for the $(Sm_{12}Co_{88})_{100-(x+y)}Nb_xC_y$ alloys—40 m/s modified with Nb as well as C.

4. Summary

Alloying of $Sm_{12}Co_{88}$ with Nb, C and combined NbC was observed to have significant effects on the microstructures and magnetic properties, while having differing effects on the magnetization processes. Nb additions led to a monotonic decrease in grain size while retaining an equiaxed grain structure.

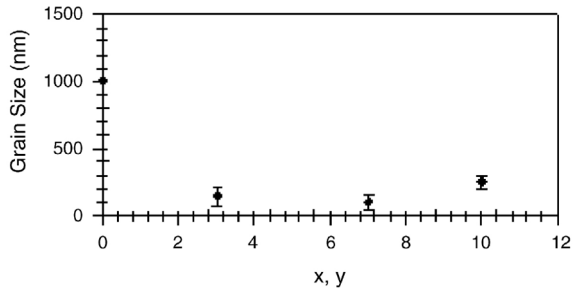

Figure 15. Relationship between grain size and concentration of additives in NbC-modified alloys.

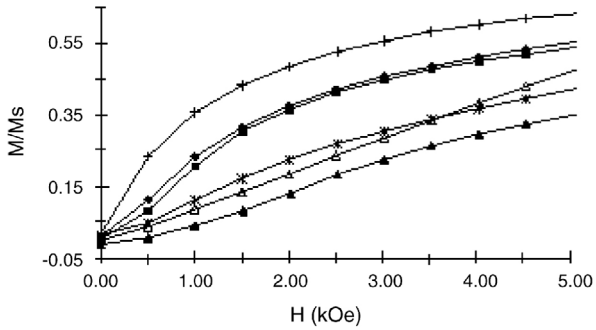

Figure 16. The normalised curves showing initial magnetization processes for the $(Sm_{12}Co_{88})_{100-(x+y)}Nb_xC_y$—40 m/s alloys modified with Nb as well as C at different (x,y) values (1,1 (♦), 2,2 (■), 3,3 (Δ), 5,5 (×) and 7,7 (▲)) and (+) is indicating the sample without any additive.

Table 1. Magnetic properties of the $Sm_{12}Co_{88}$ alloys modified with Nb and/or C

Compositions	Remanence M_r (emu/gm)	Coercivity H_c (kOe)	Maximum energy product $(BH)_{max}$ (MGOe)
$(Sm_{12}Co_{88})_{100-x}Nb_x$			
$x = 3$	50.1	9.35	6.79
$x = 5$	47.4	8.75	6.16
$(Sm_{12}Co_{88})_{100-y}C_y$			
$y = 2$	70.5	3.975	5.49
$y = 3$	56	12.03	7.75
$y = 5$	30	37.1	5.51
$(Sm_{12}Co_{88})_{100-(x+y)}Nb_xC_y$			
$x = y = 3$	52	7.75	6.68
$x = y = 5$	51.9	6.63	6.52

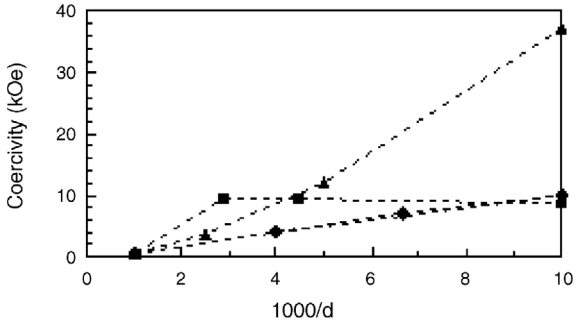

Figure 17. The dependence of coercivity on grain size for the $(Sm_{12}Co_{88})_{100-(x+y)}Nb_xC_y$—40 m/s alloys modified with Nb (■), with C (▲) and with Nb as well as C (♦).

The maximum coercivity observed was 9 kOe, and the magnetization process was predominantly nucleation-controlled. C additions, on the other hand, led to morphological changes in the grain structure, and notably the formation of a grain-boundary phase. The maximum coercivity observed with C additions was 37 kOe, and a transition to domain-wall-controlled magnetization processes was observed. The combined NbC additions led to a decrease in grain size and retained an equiaxed grain structure. The maximum coercivity observed was 8 kOe. Figure 17 represents the relationship between the observed grain size (d) and the achieved coercivity (H_c) for the alloys with all kind of additions (single (Nb or C) as well as combined (NbC)). The dependence of the coercivity on the grain size can be compared with the universal "1/d" relationship [22]:

$$H_c \propto \frac{1}{d}. \quad (1)$$

While some suggestion of domain-wall magnetization processes was observed at higher levels of alloying, the predominant magnetization process remained nucleation-controlled. In all cases the grain structure was isotropic; no preferred orientation was present. Most of the modified alloys achieved high remanence values exceeding 50 emu/g with a maximum of 70.5 emu/g. Excellent isotropic energy products were also achieved, with the best on the order of 6–8 MGOe. Table 1 represents the significant remanence and coercivity values for the different modified samples.

In conclusion, excellent as-solidified magnetic properties were achieved in Sm–Co-based alloys through minor alloying additions. No complex heat treatments were necessary to produce high coercivities, which ranged from a few kOe to almost 40 kOe.

Acknowledgements

The authors are grateful to the National Science Foundation for support of this work under Grant No. DMR0305354. Authors are grateful to the Center for Materials Research and Analysis and MRSEC: QSPINS (NSF grant no. 0213808) for facility support. Many useful discussions with L.H. Lewis, R. Skomski and R.W. McCallum are gratefully acknowledged.

References

[1] K.H.J. Buschow and A.S. vander Goot, *Acta Crystallogr. Sect. B: Struct. Crystallogr. Cryst. Chem.* **27** (1971), p. 1085.

[2] Y. Khan, *Acta Crystallogr. Sect. B: Struct. Crystallogr. Cryst. Chem.* **29** (1973), p. 2502.

[3] A.R. Yan, A. Bollero, K.H. Müller and O. Gutfleisch, *Appl. Phys. Lett.* **80** (2002), p. 1243.

[4] A. Yan, O. Gutfleisch, A. Handstein, T. Gemming and K.H. Müller, *J. Appl. Phys.* **93** (2003), p. 7975.

[5] K.D. Durst, H. Kronmüller and W. Ervens, *Phys. Status Solidi A* **108** (1988), p. 403.

[6] J. Fidler and P. Skalicky, *J. Magn. Magn. Mater.* **30** (1982), p. 58.

[7] J.D. Livingston and D.L. Martin, *J. Appl. Phys.* **48** (1977), p. 1350.

[8] I. Panagiotopoulos, T. Matthias, D. Niarchos and J. Fidler, *J. Magn. Magn. Mater.* **247** (2002), pp. 355–362.

[9] M.F. Rhen Farnando, M. Venkatesan, I.R. Harris and J.M.D. Coey, *J. Appl. Phys.* **93** (2003), p. 8683.

[10] A.R. Yan, Z. Sun, B. Han and B. Shen, *J. Mater. Res.* **17** (2002), p. 648.

[11] A.R. Yan, W.Y. Zhang, H.W. Zhang and B.G. Shen, *J. Magn. Magn. Mater.* **210** (2000), p. L10.

[12] A.R. Yan, A. Bollero, K.H. Müller and O. Gutfleisch, *J. Appl. Phys.* **91** (2002), p. 8825.

[13] I. Tung, H. Zhang, S. Yao, J. Shih, B. Shen and T. Chin, *J. Phys. D: Appl. Phys.* **32** (1999), p. 1587.

[14] S.S. Makridis, G. Litsardakis, I. Panagiotopoulos, D. Niarchos, Y. Zhang and G.C. Hadjipanayis, *IEEE Trans. Magn.* **38** (2002), p. 2922.

[15] W. Manrakhan, L. Withanawasam, X. Meng-Burany, W. Gong and G.C. Hadjipanayis, *IEEE Trans. Magn.* **33** (1997), p. 3898.

[16] J.E. Shield, V.K. Ravindran, S. Aich, A. Hsiao and L.H. Lewis, *Scripta Materialia* **52** (2005), pp. 75–78.

[17] S. Aich, J. Kostogorova and J.E. Shield, *J. Appl. Phys.* **97** (2005), pp. 1–3 10H108.

[18] K.H.J. Buschow and A.S. vander Goot, *Acta Crystallogr. Sect. B: Struct. Crystallogr. Cryst. Chem.* **27** (1971), p. 1085.

[19] *ASM Handbook* **vol.3**, ASM International, Materials Park, OH (1997) p. 2.148.

[20] V.K. Ravindran, MS thesis, University Of Nebraska, Lincoln, 2005.

[21] S. Aich, V.K. Ravindran, J.E. Shield, J. Appl. Phys., in press.

[22] T. Sun, *J. Appl. Phys.* **52** (1981), p. 2532.